GSA Data Repository 2019056

Deformation driven by deep and distant structures: Influence of a mantle lithosphere suture in orogen development

Philip J Heron[1], R.N. Pysklywec[2], R. Stephenson[3], J. van Hunen[1]

Contents:

Supplemental Methods

ASPECT is a geodynamic modelling code that uses the finite-element method to solve the system of equations that describes the motion of a highly viscous fluid. Detail of the code that isn't directly related to the modelling setup specific to this study can be found in the ASPECT user manual (Bangerth et al., 2018) and a recent ASPECT canonical publication (Heister et al., 2017). Computations were done using the ASPECT code version 2.0.0, see Heister et al., 2017, Bangerth et al., 2018, Kronbichler et al., 2012 and Rose et al., 2017.

Experimental setup

The three-dimensional numerical experiments conducted in this manuscript are within a Cartesian box of 800 km (x-axis) by 800 km (y-axis) and 600 km vertically (z-axis). The computational grid that solves the visco-plastic Stokes equations is shown in Fig. DR2. The computational grid is fixed laterally but varies vertically, with higher resolution prescribed in the top 80 km of the model (from the surface to 80 km depth). Below, the resolution becomes coarser, with a reduction in resolution between 80 and 180 km, then finally lower resolution from 180 km depth to the bottom of the model (Fig. DR1). There are 1.7 million active cells in the model, with a resolution of ~1 km at the surface.

The 3D simulations are very computationally expensive, producing 147 million degrees of freedom and needing around 80 GB memory. For most cases, the models used 416 CPUs and took ~16,000 hours of computational time to generate 12 Myr of deformation on ComputeCanada's Niagara cluster.

Governing equations

In this study, we solve the equations of conservation of momentum, mass and energy after assuming an incompressible medium with infinite Prandtl number:

$$-\nabla \cdot \left(2\mu \dot{\boldsymbol{\varepsilon}}(\boldsymbol{u})\right) + \nabla \mathrm{p} = \mathrm{p}\mathbf{g}$$
$$\nabla \cdot \boldsymbol{u} = 0$$
$$\rho C_p\left(\frac{\partial T}{\partial t} + \boldsymbol{u} \cdot \nabla \mathrm{T}\right) - \nabla \cdot k \nabla \mathrm{T} = \rho H.$$

In the equations above, μ is the viscosity, $\dot{\boldsymbol{\varepsilon}}$ is the strain rate tensor, u is the velocity vector, k is the thermal conductivity, ρ is the density, C_p is the thermal heat capacity, α is the thermal expansivity, H the internal heat production, and T the temperature. The strain rate tensor is given as:

$$\dot{\boldsymbol{\varepsilon}} = \frac{1}{2}(\nabla \boldsymbol{u} + \nabla \boldsymbol{u}^T).$$

Different material parameters (in this case upper crust, lower crust, mantle lithosphere, asthenosphere, etc.) are represented by *compositional fields* that are advected with the flow

(similar to the temperature field). For each field c_i, this formulation introduces an additional advection equation to the system of equations:

$$\frac{\partial c_i}{\partial t} + \boldsymbol{u} \cdot \nabla c_i = 0$$

The equations above are solved using the finite element method, where the domain is discretized into quadrilateral/hexahedral finite elements and the solution (e.g., velocity, pressure, temperature and compositional fields) is expanded using Lagrange polynomials as interpolating basis functions (as outlined in Glerum et al., 2017). In this study, we employ second order polynomials for velocity, temperature and composition and first order polynomials for pressure (Q_2Q_1 elements, e.g. Donea and Huerta, 2003). The equations are solved using an iterative Stokes solver (for more details see Kronbichler et al., 2012).

The ASPECT material field *visco-plastic* was used for this study, which is an implementation of a visco-plastic rheology with options for selecting dislocation creep, diffusion creep or a composite viscous flow law. Plasticity limits viscous stresses through a Drucker Prager yield criterion. The model is incompressible, but we apply the real density to the temperature equation.

The viscosity for dislocation or diffusion creep is defined as:

$$\mu = 0.5A^{-\frac{1}{n}} \dot{\varepsilon}_{ii}^{\frac{(1-n)}{n}} \exp\left(\frac{E+PV}{nRT}\right)$$

where A is the prefactor, n is the stress exponent, $\dot{\varepsilon}_{ii}$ is the square root of the deviatoric strain rate tensor second invariant, E is activation energy, V is activation volume, P is pressure, R is the gas exponent and T is temperature (e.g., Billen and Hirth, 2007). Here, we select to use the dislocation creep ($v_{(disl)}; n > 1$) equation form.

Viscosity is limited through one of two different 'yielding' mechanisms. Plasticity limits viscous stress through a Drucker Prager yield criterion, where the yield stress in 3D is

$$\boldsymbol{\sigma_y} = \{\boldsymbol{6C\cos\varphi + 2P\sin\varphi}\}/\{\sqrt{\boldsymbol{3}}(\boldsymbol{3+\sin\varphi})\}.$$

Above, C is cohesion and $\boldsymbol{\varphi}$ is the angle of internal friction. If $\boldsymbol{\varphi}$ is 0, the yield stress is fixed and equal to the cohesion (Von Mises yield criterion). When the viscous stress ($2\boldsymbol{\mu\varepsilon_{ii}}$) exceeds the yield stress, the viscosity is rescaled back to the yield surface $\boldsymbol{\mu_y} = \boldsymbol{\sigma_y}/(2\dot{\boldsymbol{\varepsilon}}_{\boldsymbol{ii}})$, (e.g., Thieulot, 2011). This method of plastic yielding known as the Viscosity Rescaling Method (VRM) (Willett, 1992; Kachanov, 2004) and is implemented by locally rescaling the effective viscosity in such a way that the stress does not exceed the yield stress. In the models here, strain weakening is implemented for the internal friction angle and cohesion – they are linearly reduced by 50% of their value as a function of the finite strain magnitude (from 0.5 to 1.5) (Table DR1).

Compositional fields (upper crust, lower crust, mantle lithosphere, asthenosphere, and scarring) can each be assigned individual values of thermal diffusivity, heat capacity, density, thermal expansivity and rheological parameters (Table DR1). If more than one compositional field is present at a given point (such as for a scar overlain on top of mantle lithosphere), viscosities are averaged with a harmonic scheme (e.g., Glerum et al., 2017).

An initial reference viscosity of 1e+22 *Pa.s* is applied to each compositional field in the models due to the strain rate dependence of viscosity and the lack of an initial guess for the strain rate for the first time-step (Glerum et al., 2017). This initial reference viscosity is starting point to calculate the different viscosity at depth. In testing, we have modified the initial reference viscosity up and down by two orders of magnitude and found no difference in the final outcome of the simulations. During subsequent time-steps, the strain rate of the previous time-step is used as an initial guess for the iterative process. The final effective viscosity is capped by a (user-defined) minimum viscosity (set at 1e+18 Pa.s) and maximum viscosity (set at 1e+26 Pa.s) to avoid extreme excursions and to ensure stability of the numerical scheme. In the models presented here, we apply a viscosity range of 8 orders of magnitude. However, for the majority of models the viscosity profile stays well within this range.

Lithosphere scarring

In the models presented in the main manuscript, the mantle lithosphere scar has a dip of 15 degrees from the horizontal and extends to a depth of 52 km from the initial starting point 32 km down. This shallow dip is consistent with that indicated from seismic imaging (Mickus and Keller, 1992). The mantle lithosphere scar is presumed to be a weak feature, possibly from grain damage processes through ancient deformation. The weakness of the scar is given by prescribing a low value to the internal angle of friction on the structure (1^{o}) – all other rheological properties are the same as the rest of the layer. In a previous 2D study, the influence of how weak a mantle lithosphere scar needs to be (e.g., changing the value for the angle of internal friction) in the presence of crustal scars was rigorously tested (Heron et al., 2016). Here we have compared our new model with these previous studies and performed new models in three dimensions. For models UC and UC-ML (and UC2 and UC2-ML), the upper crustal scars have the same properties as the upper crust but with a 1^{o} angle of internal friction.

Time stepping

Here, we use the Courant-Friedrichs-Lewy (CFL) condition to ensure stable convergence. In these calculations the CFL criterion is set to 0.5. However, we have tested the model with

smaller CFL values to ensure the setup is robust.

Rheologies

The rheological setup of these models closely follows that of Naliboff and Buiter (2015). Table DR1 outlines the rheological parameters used for the different compositional layers. The upper crust implements a wet quartzite flow law (Rutter and Brodie, 2004), lower crust applies wet anorthite (Rybacki et al., 2006), and the mantle dry olivine (Hirth and Kohlstedt, 2004). All the viscous pre-factors described in Table DR1 are scaled to plane strain from unixial strain experiments.

Boundary conditions

In the models presented here, we apply a prescribed boundary velocity on the north and south boundaries, and tangential velocity boundary condition on the west, east and base walls of the model, and a free surface on top. We have modelled the Cartesian 3D box large enough so that deformation driven from the scarring is not influenced by the tangential boundary conditions (as described below).

The prescribed boundary condition on the north wall is a 1 cm/yr convergence for the lithosphere (120 km) and a return flow of -0.6 cm/yr for the bottom 200 km of the box. In between, the velocity tapers from 1 cm/yr to 0 cm/yr from 120 km to 225 km depth, and from 0 cm/yr to -0.6 cm/yr from 200 km to 400 km depth. The reverse is applied to the west wall, with 1 cm/yr compression for the lithosphere. After extensive testing, we found this boundary condition to provide stable solutions.

The free surface is formulated by an Arbitrary Lagrangian-Eulerian (ALE) framework for handling motion of the mesh (for more details please refer to Bangerth et al., 2017). All the calculations presented here have 5,566,239 free surface degrees of freedom.

Thermal model setup

An initial temperature field is prescribed (Fig. DR1a) but is allowed to evolve during the simulation (Fig. DR1b). The initial temperature follows a typical continental geotherm (Chapman, 1986) with no lateral variations. Our initial condition models late Paleozoic convergence of two connected continental blocks, which first collided in the Proterozoic (Fig 1Ci-1Cii). The last closure of the oceanic basin to accrete the Sabine Block to the Laurentian occurred over 1 Ga in the past (Dunn, 2009; Fig 1Cii), and therefore there are no thermal perturbations from the tectonic event remaining. Table DR2 gives the values for the thermal constraints required to generate the geotherm. As described in Naliboff and Buiter (2015), we use a high conductivity in the asthenosphere to maintain the high adiabat in the layer, and to generate a constant heat flux into the lithosphere (Pysklywec and Beaumont, 2004).

The temperature equation for calculating the initial geotherm is given as follows:

$$T(z) = T_o + \frac{q}{k}z - Hz^2/2k$$

where T_o is the temperature at the top of the specific layer, H the heat production, q the heat flow through the surface of the specific layer, k the thermal conductivity and z the depth.

Model Results

Fig DR2-5 shows further information regarding the main model *ML*, including the initial temperature and viscosity condition (Fig DR2). The surface strain evolution and topography for the model run is shown in Fig DR3 and DR4, respectively. The deformation front as shown in the main manuscript (Fig 2) forms early in the model run (Fig DR3). To understand further the importance of the mantle lithosphere heterogeneity, we present the vertical component of model velocity at different depths for *Model ML* after 4 Myr (Fig. DR5). Near the surface at 5 km depth (Fig. DR5A), there is a complex pattern of uplift and subsidence in the upper crust. Deeper in the lithosphere, the pattern of the vertical velocity becomes simpler and larger in magnitude. In the lower crust, there is a broad zone of downward pull with a relatively narrow zone of uplift, representing the thrust front (Fig. DR5B). At 35 km depth, in the mantle lithosphere, the downward pull is strong, with the mantle lithosphere scar acting as a locus of deformation along which the lithosphere moves. The relatively simple process at depth produces a complex pattern of tectonic deformation at the surface.

Fig DR6 presents a direct comparison of the main result from *Model ML* with the surface geology features of the Ouachita orogeny. For easy comparison, we have scaled the Ouachita deformation to our model region through matching the size of the Sabine Block outline from Fig 1A to our model mantle scar outline. Fig DR6 shows the Ouachita deformation front in white as compared our model front in red, with corresponding Arkoma and Fort Worth basins in dashed purple bounding the front to the north and west. The extra deformation limb in the east of the Ouachita deformation front may be due to our model mantle lithosphere structure being perpendicular to the convergence direction in that region (highlighted by 'A' in Fig. DR6). The Sabine Block may have a more oblique outline to it than our model (highlighted by 'B' in Fig. DR6),

In Fig DR7, we present the impact of changing the mantle lithosphere scar angle on the deformation of the orogeny. A feature of the Ouachita orogeny is the varying offset of ~100 – 200 km between mantle lithosphere structure and main thrust front (Keller and Hatcher, 1999). This may be explained by a changing mantle lithosphere scar angle across the orogen – in Fig. DR7 we demonstrate that shallow dipping mantle structures can generate a greater offset from mantle to crust than a steeply dipping feature (although the difference is small in this example).

In Fig. DR8 we present the impact of a mantle lithosphere scar in the presence of another set of inherited crustal structures (*Model UC2*) – in particular, a set of weak upper crustal faults (Fig. DR8A) positioned in relation to prior rift tectonics (e.g., Thomas, 2010; Calignano et al., 2017). In keeping with *Model UC* (Fig 3), the upper crustal scarring fails to localize deformation across the model region (Fig DR8B). However, the presence of the mantle lithosphere scar (Fig DR8C) controls the tectonics over the shallow features and localizes deformation (Fig DR8D).

Experiment Sensitivity and Robustness

In the formulation of this manuscript, we experimented with the sensitivity of the input parameters and how robust the results are. First, we benchmarked the ASPECT numerical code against previous 2D simulation of visco-plastic models of lithosphere deformation. In 2D, we compared our ASPECT models with that of published work with the numerical code SOPALE. In 2D, the role of mantle lithosphere scarring has been extensively analysed in a parameter space study with SOPALE (Heron et al., 2016). We found that the numerical simulations in ASPECT compared well with that of SOPALE, which gave us the confidence to pursue 3D simulations of visco-plastic deformation.

To ensure the results presented here are robust, we implemented a number of supplementary models (Table DR3). In particular, we ran a full suite of models using different strain weakening parameters. In the test suite, strain weakening is implemented for the internal friction angle only – it is linearly reduced as a function of the finite strain magnitude (where it is decreased from $\mathbf{20^o \rightarrow 5^o}$, between a 0 and 1.0 strain range). The weak scar has an internal angle of friction of zero. However, the test *Model ML* shows very similar results to those shown in the main manuscript.

To further examine the robustness of the study, we have also tested the role of: strain weakening in cohesion and internal angle of friction; the reference strain rate; the reference viscosity; the CFL condition; a composite diffusion creep/dislocation creep asthenosphere; the positioning of the mantle scar from the centre of the model; the size of the box; rate of convergence; application of artificial diffusivity; lower crustal strength; scar length; and scar angle (amongst others). We do not present these models here as they would be repetitive and take up too much space. However, we do provide a list of the models that were conducted, with notes as to how they deviate from the main model, *Model ML*. The model which impacted the overall results shown by *Model ML* was the use of a strengthened mantle lithosphere scar (which did not localize deformation). In analysing the topography of the test models (Fig DR9A and DR9B), *Model T-Vel* (increased convergent velocity), T-*SW* (both cohesion and internal angle of friction strain weakening), and T-*Coh* (only cohesion strain weakening rather than just internal angle of friction strain weakening) show a deviation from the reference *Model T-ML*'s maximum and minimum topography. However, the overall deformation pattern between *T-Vel, T-SW* and *T-Coh* are broadly similar to *ML*.

Supplementary Tables and Figures

Property	Units	UC	LC	ML	A	ML Scar
Density	$kg\ m^{-3}$	2800	2900	3300	3300	3300
Thermal diffusivities	$m^2\ s^{-1}$	1.90476e-6	1.149425e-6	1.33333e-6	1.33333e-6	1.33333 e-6
Viscosity prefactor (A*)	$Pa^n\ m^{-p}\ s^{-1}$	8.57e-28	7.13e-18	6.52e-16	6.52e-16	6.52e-16
Stress exponent, n		4.0	3.0	3.5	3.5	3.5
Activation energies (Q)	$kJ\ mol^{-1}$	223e3	345e3	530e3	530e3	530e3
Activation volumes	$m^3\ mol^{-1}$	0.	0.	18e-6	18e-6	18e-6
Thermal expansivities	K^{-1}	2e-5	2e-5	2e-5	2e-5	2e-5
Specific heat	$J\ kg^{-1}\ K^{-1}$	750	750	750	750	750
Heat production	$W\ m^{-3}$	1.5e-6	0	0	0	0
Angles of internal friction	^{o}	20 -> 10	20 -> 10	20 -> 10	20 -> 10	1-> 0.5
Cohesions	Pa	20e6 -> 10e6	20e6 -> 10e6	20e6 -> 10e6	20e6 -> 10e6	20e6 -> 10e6

Table DR1. Rheological parameters for *Model ML*. Angles of internal friction have strain weakening properties. For models UC and UC-ML, the upper crustal scars have the same properties as the upper crust above, but with a 1 ^{o} angle of internal friction. Strain weakening occurs over the range 0.5 to 1.5, in keeping with Naliboff and Buiter (2015).

Property	Units	UC	LC	ML	A
Width	km	20	10	90	480
Temp top of layer surface	℃	0	409	500	1300
Layer surface heat flow	W/m^2	0.0653571	0.035357	0.0275	0.0126582
Thermal conductivity	$W/(m\ K)$	2.5	2.5	3.3	39.25
Heat production	W/m^3	1.6e-6	0	0	0

Table DR2. Thermal parameters for all initial temperature profiles for computing the continental geotherm.

#	Name	Dim	Where	Description
1	*ML*	3D	Fig 2-3	Main model as described in text
2	*UC*	3D	Fig 3	UC scars
3	*UC-ML*	3D	Fig 3	UC scars and ML scar
4	*UC2*	3D	DR	Another set of UC scars
5	*UC2-ML*	3D	DR	UC2 with ML scar
6	*Zero*	3D	NS	No scars – no localization
7	*Dip*	3D	DR	Angled scar dip
8	*Strength*	3D	NS	ML scar that is strong - no localization
9	*Simple*	3D	NS	No limbs on the ML scar
10	*T-ML*	2D	DR	Test suite setup – only 50% strain weakening and 0 degree weak scar angle of internal friction. This is the setup for all the T- models unless specified.
11	*T-Vel*	3D	DR	Increased convergence to 2cm/yr
12	*T-Diff*	3D	DR	Diffusion creep asthenosphere
13	*T-Coh*	3D	DR	Cohesion strain weakening
14	*T-Visc 1*	3D	NS	Reference viscosity increased to 1E+23
15	*T-Visc 2*	3D	NS	Reference viscosity increased to 1E+21
16	*T-SR*	3D	DR	Reference Strain rate decrease to 1E-17
17	*T-CFL*	3D	DR	CFL reduced to 0.25
18	*T-Art Diff*	3D	NS	Application of artificial diffusivity
19	*T-SW*	3D	DR	Strain weakening 50% for cohesion and friction
20	*Dip*	3D	DR	Steeper angle of ML scar
21	*Box*	3D	NS	Increasing box width
22	*Pos*	3D	NS	Changing position of ML scar
23	*LC rhe*	3D	NS	Changing LC rheology for ML model
24	*Scar steep*	3D	DR	Short ML scar that is steep
25	*Scar shallow*	3D	DR	Short ML scar that is shallow
26	*UC-ML**	3D	DR	UC scars and ML scar with internal friction angle = 0^o
27	*2DML*	2D	DR	Scarring set up as Heron et al., 2016
28	*UC-ML***	3D	DR	UC scars and ML scar with internal friction angle = 10^o
29	*LC-ML***	3D	DR	LC scars and ML scar with internal friction angle = 10^o
		3D	NS	Various different scar geometries

Table DR3. List of some of the numerical models performed in this study: *DR* denotes the model features in the Data Repository; *NS* denotes the models were not shown and were run for testing purposes. All testing models presented results similar to those described in the text (unless specified in description).

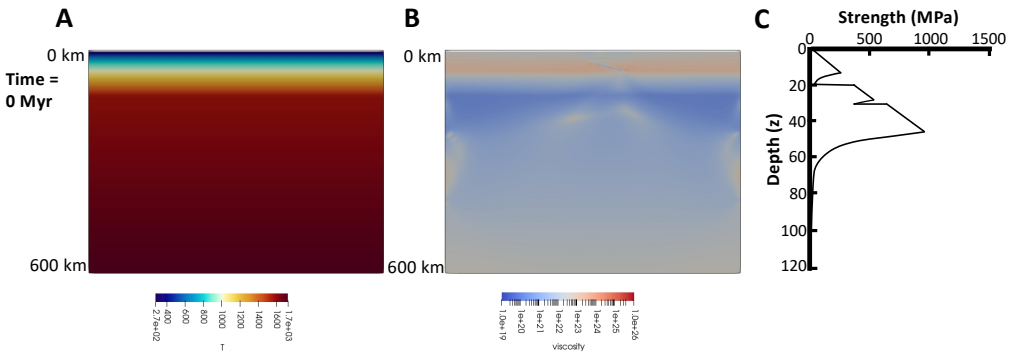

Figure DR1. Temperature (A) and viscosity (B) profile in a slice across the middle of the box (N-S) for *Model ML*. The lithosphere strength profile for the heterogenous mantle is given in (C), with a strain rate of 1e-14 s^{-1} and the rheological parameters as given in Table DR1.

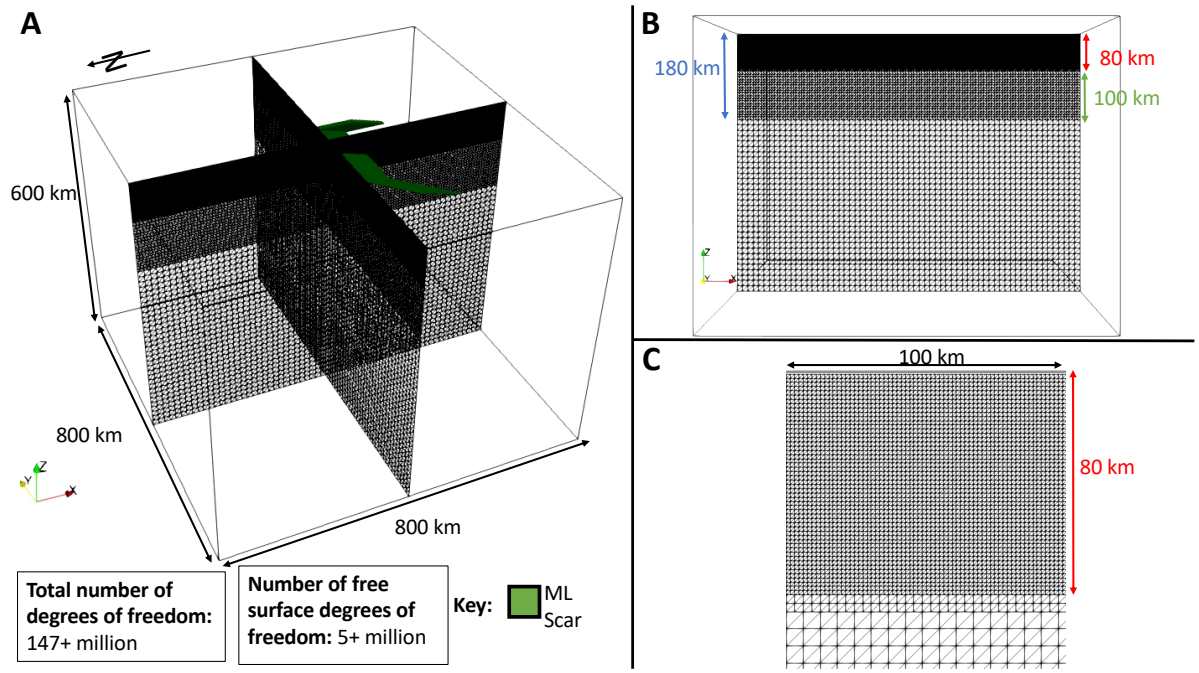

Figure DR2. Finite element fixed mesh for all models. There are 1.7 million active cells in the model, with a resolution of ~1 km at the surface.

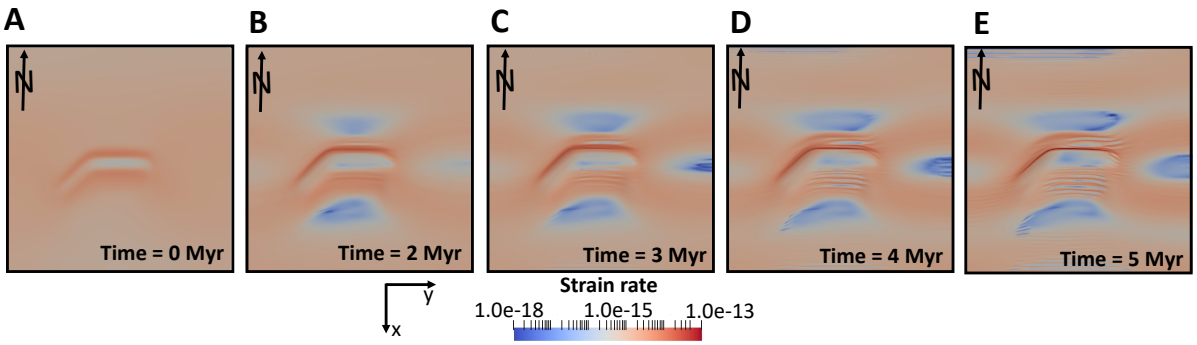

Figure DR3. Model evolution of surface strain rate for *Model ML*.

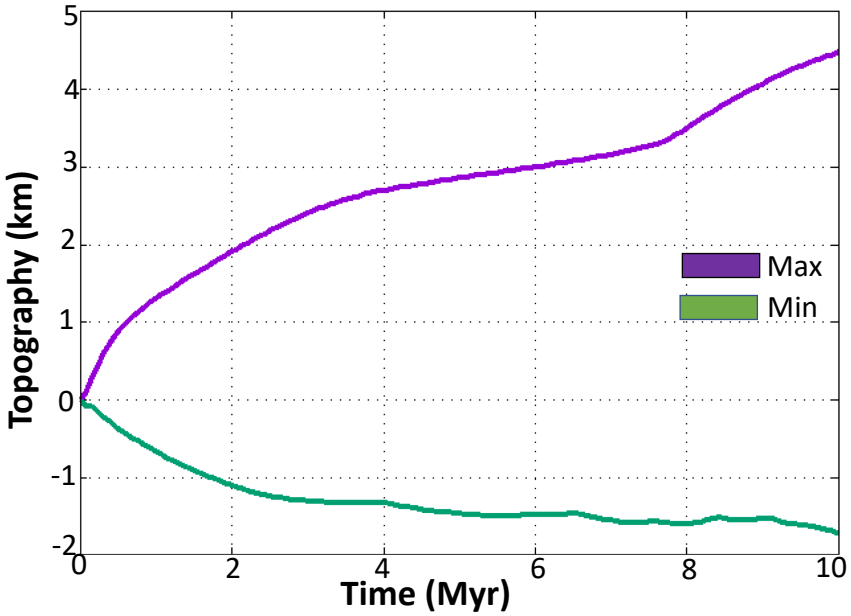

Figure DR4. Maximum and minimum topography evolution for *Model ML*.

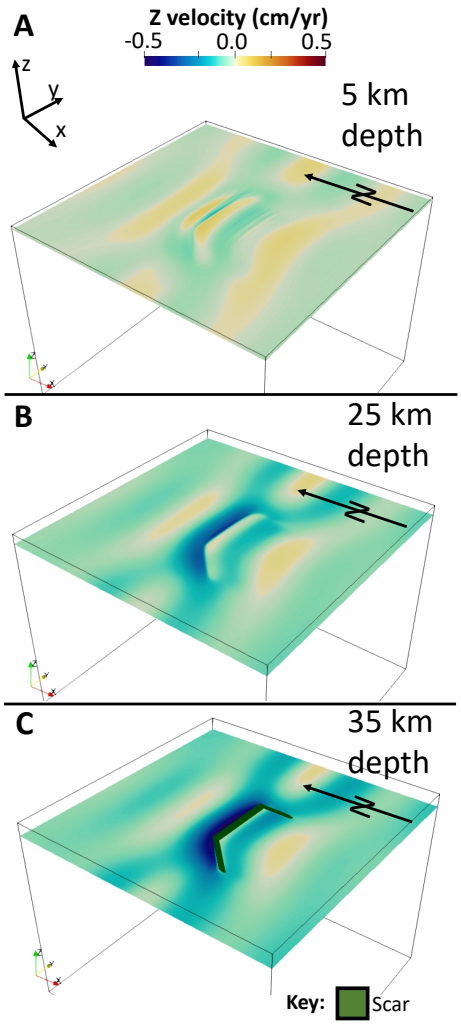

Figure DR5. Slices of the vertical velocity component of lithosphere deformation for *Model ML* after 4 Myr of compression (80 km) at **A:** 5 km depth (upper crust), **B:** 25 km depth (lower crust) and **C:** 35 km depth (mantle lithosphere).

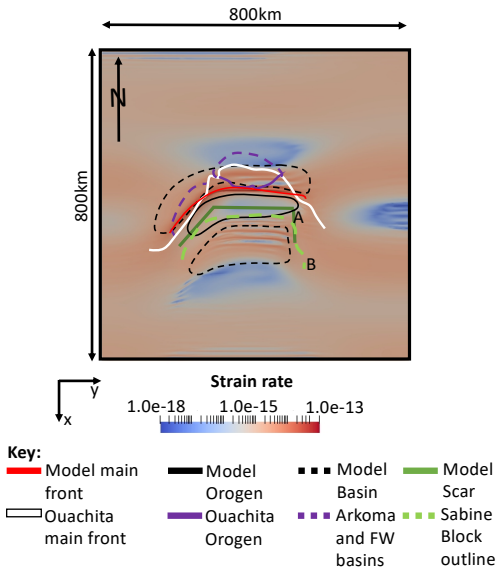

Figure DR6. Comparison between the geological surface expressions of the Ouachita orogeny and the deformation of *Model ML*. Background figure is from Fig 2C in the main manuscript, with *Model ML* surface strain rate after 4 Myr with model orogen, basin and deformation front highlighted alongside mantle scar original location. Here, the regional Ouachita tectonics are scaled to our models by matching the outline of the Sabine Block with our model scar. The deformation patterns of the arcuate orogeny and basin development occur in similar positions for our model and the geophysical and geological data. In Key, FW denotes Forth Worth. For explanation of 'A' and 'B' please refer to text.

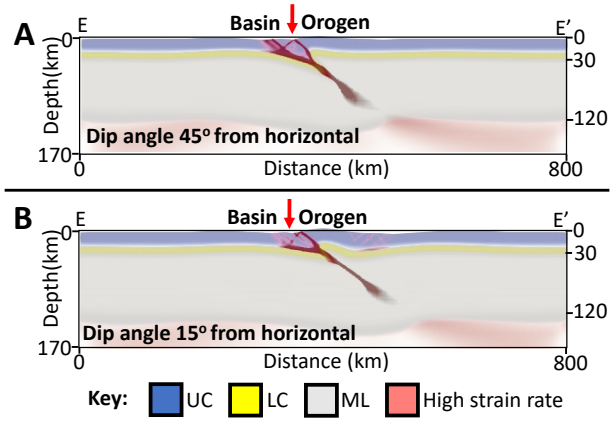

Figure DR7. Cross-section view of *Model Dip* (A) and *Model ML* (B) across the middle of the orogeny (E-E', Fig 2) after 4 Myr of compression. The models compare the differences between in deformation patterns when the dip angle becomes steeper. There is a small change in orogeny position, with slight differences in tectonic deformation (high strain rate).

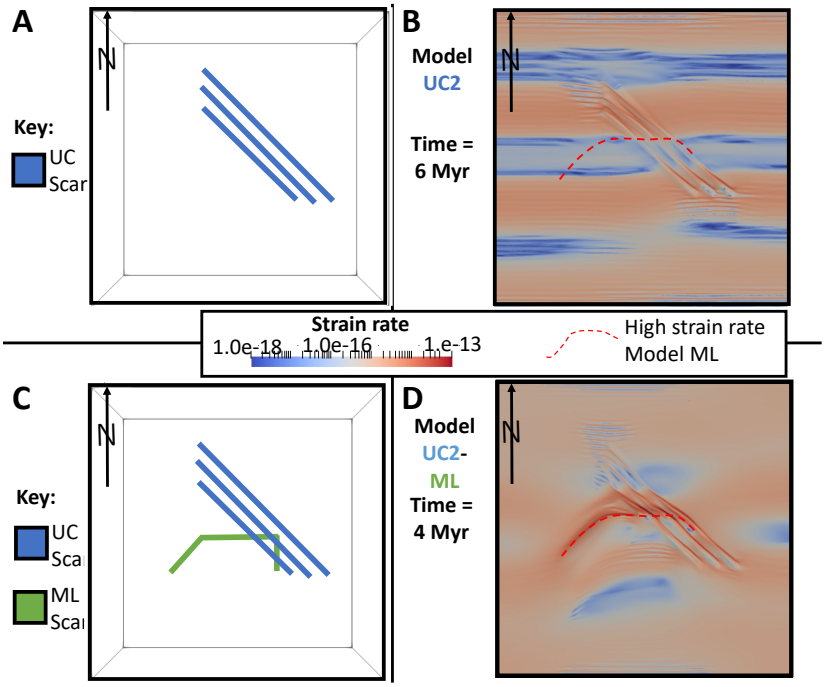

Figure DR8. Top down view of the surface strain rate for models featuring mantle lithosphere scars and crustal heterogeneities (the main deformation front for *Model ML* is given by dashed red line). **A:** Outline of the upper crustal scarring for *Model UC2* (featuring just the UC scars), with corresponding strain rate plots for **B:** *Model UC2* (at 6 Myr). In *Model UC2*, the deformation does not localize across the region. **C:** Outline of the upper crustal and mantle lithosphere scarring for *Model UC2-ML*, with corresponding strain rate plots for **D:** *Model UC2-ML* (at 4 Myr). Here, the mantle lithosphere scar dominates crustal tectonics early in the model evolution.

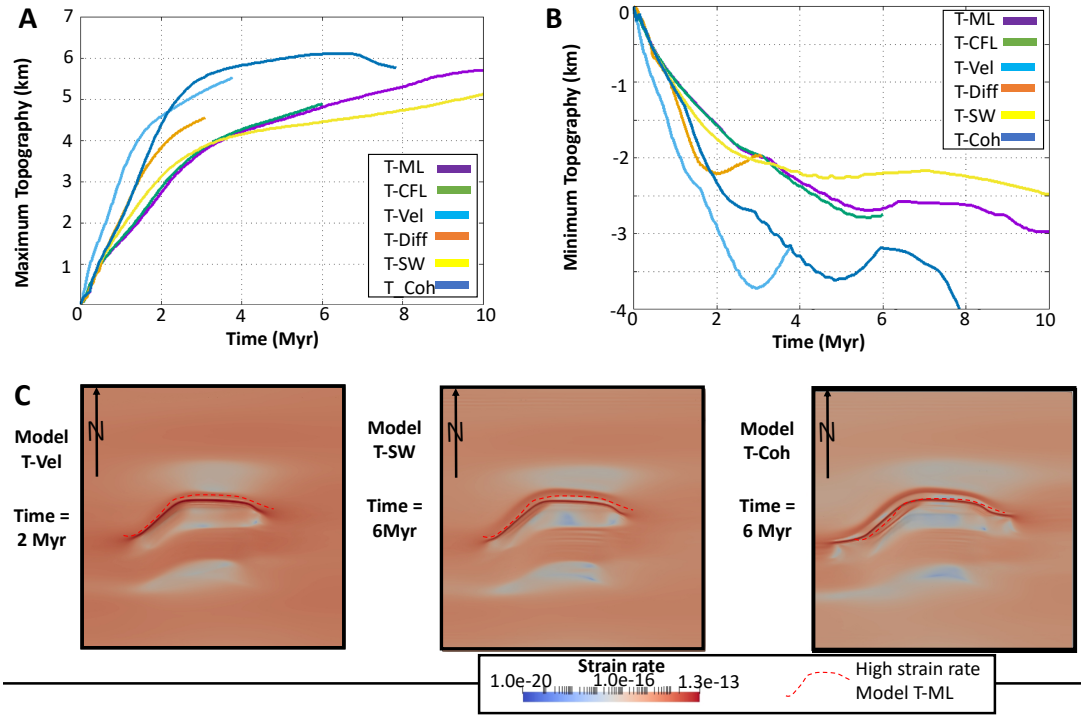

Figure DR9. Testing the robustness of the results. A full suite of models was conducted with different strain weakening parameters, and comparison between some of these testing models are shown. See Table DR3 for model descriptions. **A:** maximum and **B:** minimum topography values for the test models. **C:** comparison of surface strain rate plots for Model T-Vel, Model T-Coh, and Model T-SW. Models that show a large deviation from the Model T-ML maximum and minimum topography (T-Vel, T-SW, T-Coh), do not show much change in the actual deformation patterns.

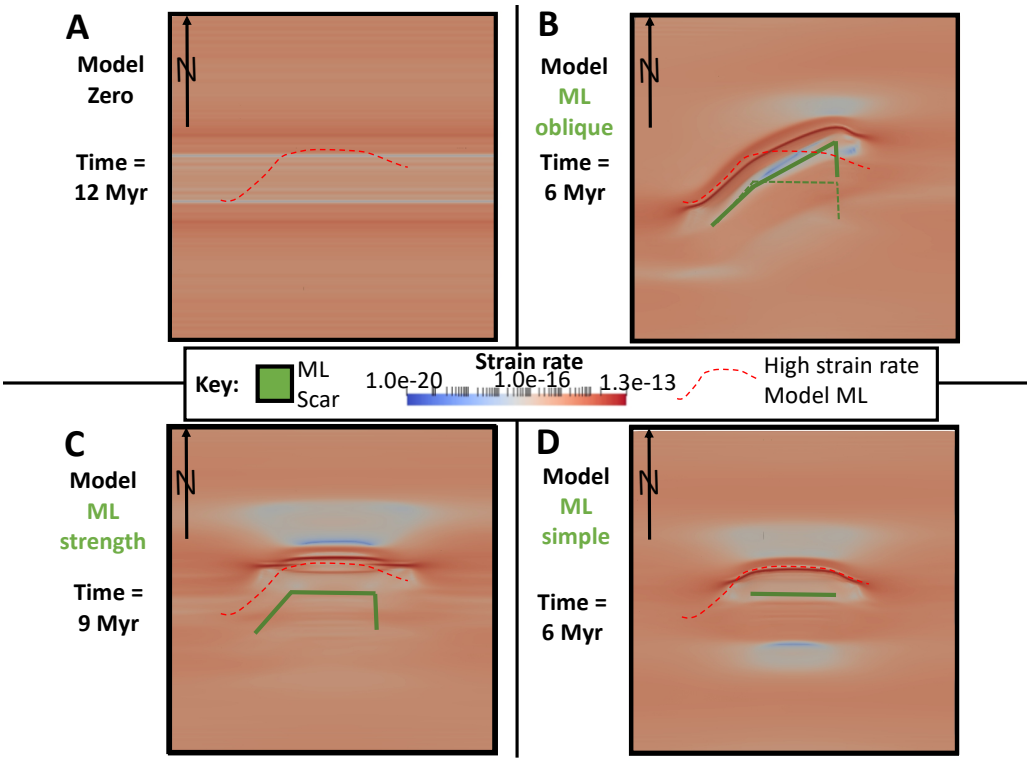

Figure DR10. Top down view of surface strain rate of additional models. A: Model with no scarring. B: Model with oblique scarring (original position of ML scar given in green, with original Model ML scar shown in dashed green). C: Model with ML scar that has strength rather than weakness. D: ML scar without the east and west limbs. Dashed red line outlines the main front of the reference Model ML at 6 Myr.

Code and experimental inputs

Numerical code used
For these calculations we used ASPECT version 2.0, with dealii version 8.5.1. The version of ASPECT used can be found here
https://github.com/geodynamics/aspect

Another webpage for the ASPECT code can be found here:
https://aspect.geodynamics.org

The manual for the code has more detail about the inner workings and formulations, as well as information on benchmarking. The manual is available here:
http://www.math.clemson.edu/%7Eheister/manual.pdf - updated regularly (currently 30 MB and 454 pages).

Experimental inputs

The experiments were designed from the continental extension ASPECT cookbook: https://github.com/geodynamics/aspect/blob/master/cookbooks/continental_extension.prm
The input files for this experiment can be found here:
https://github.com/heronphi/Heron_etal2019

References

Bangerth, W., Dannberg, J., Gassmoeller, R., & Heister, T. (2018, May 10). Aspect V2.0.0. Zenodo. https://doi.org/10.5281/zenodo.1244587

Billen M.I., Hirth G. 2007. Rheologic controls on slab dynamics. Geochem. Geophys. Geosyst. 8:Q08012, doi: 10.1029/2007GC001597

Dunn, D.P., 2009, Arkansas crustal xenoliths: Implications for basement rocks of the northern Gulf Coast, USA: Lithosphere, v. 1, p. 60–64, https://doi.org/10.1130/L10.1.

Calignano, E., Sokoutis, D., Willingshofer, E., Brun, J.-P., Gueydan, F.,and Cloetingh, S., 2017, Oblique contractional reactivation of inherited heterogeneities: Cause for arcuate orogens, Tectonics, 36, 542–558, doi:10.1002/2016TC004424.

Cížková, H., Bina, C.R., 2013. Effects of mantle and subduction-interface rheologies on slab stagnation and trench rollback. Earth Planet. Sci. Lett. 379, 95–103. http://dx.doi.org/10.1016/j.epsl.2013.08.011.

Cížková, H., Bina, C.R., 2015. Geodynamics of trench advance: insights from a philippine-sea-style geometry. Earth Planet. Sci. Lett. 430, 408–415.

Chapman, D., 1986. Thermal gradients in the continental crust. In: Dawson, J., Carswell, D., Hall, J., Wedepohl, K. (Eds.), The Nature of the Lower Continental Crust, vol. 24. Geol. Soc. Spec. Publ., pp. 63–70.

Christensen, U.R., 1992. An Eulerian technique of thermomechanical modeling of lithospheric extension, J. geophys. Rex, 97, 2015-2036.

Donea, J. and Huerta, A., 2003, Finite element methods for flow problems, John Wiley & Sons, Ltd, doi:10.1002/0470013826.

Glerum, A., Thieulot, C., Fraters, M., Blom, C., and Spakman, W., 2017, Implementing nonlinear viscoplasticity in ASPECT: benchmarking and applications to 3D subduction modeling, Solid Earth Discuss., https://doi.org/10.5194/se-2017-9.

Heister, T., Dannberg, J., Gassmoller, R., Bangerth, W., 2017, High accuracy mantle convection simulation through modern numerical methods – II: realistic models and problems. Geophys. J. Int. 210, 833–851.

Heron, P. J., R. N. Pysklywec, and R. Stephenson, 2016, Identifying mantle lithosphere inheritance in controlling intraplate orogenesis, J. Geophys. Res. (Solid Earth), 6966–6987, doi:10.1002/2016JB013460.

Hirth, G. and Kohlstedt, D., 2003, Rheology of the upper mantle and the mantle wedge: a view from the experimentalists. In: Eiler, J. (Ed.), Inside the Subduction Fac- tory. In: Geophys. Monogr. Am. Geophys. Soc., vol. 138, pp. 83–105.

Kachanov, L. M., 2004, Fundamentals of the Theory of Plasticity, Dover Publications, Inc..

Keller, G.R., and Hatcher, Jr., R.D., 1999, Some comparisons of the structure and evolution of the southern Appalachian-Ouachita orogen and portions of the Trans-European suture zone region, in H. Thybo, T.C. Pharaoh, and A. Guterch, (eds.), Geophysical investigations of the Trans-European suture zone: Tectonophysics, v. 314/1-3, p. 43-68.

Kronbichler, M., Heister, T., and Bangerth, W., 2012, High accuracy mantle convection simulation through modern numerical methods, Geophysical Journal International, 191, 12–29.

Mickus, K. L., and Keller, G. R., 1992, Lithospheric structure of the south-central United States, Geology, 20, 335–338, doi:10.1130/0091-7613.

Naliboff, J., and S. J. H. Buiter, 2015, Rift reactivation and migration during multiphase extension, Earth Planet. Sci. Lett., 421, 58–67, doi:10.1016/j.epsl.2015.03.050.

Pysklywec, R., Beaumont, C., 2004, Intraplate tectonics: feedback between radioactive thermal weakening and crustal deformation driven by mantle lithosphere instabilities. Earth Planet. Sci. Lett. 221, 275–292.

Rose, I., Buffett, B., & Heister, T. (2017). Stability and accuracy of free surface time integration in viscous flows. Physics of the Earth and Planetary Interiors, 262, 90–100. doi:10.1016/j.pepi.2016.11.007

Rutter, E., and Brodie, K., 2004, Experimental grain size-sensitive flow of hot-pressed Brazilian quartz aggregates. J. Struct. Geol. 26, 2011–2023.

Rybacki, E., Gottschalk, M., Wirth, R., Dresen, G., 2006, Influence of water fugacity and activation volume on the flow properties of fine-grained anorthite aggregates. J. Geophys. Res. 111 (B3).

Thieulot, C., 2011, FANTOM: Two- and three-dimensional numerical modelling of creeping flows for the solution of geological problems, Physics of the Earth and Planetary Interiors, 188, 47–68.

Thomas, W.A., 2010, Interactions between the southern Appalachian–Ouachita orogenic belt and basement faults in the orogenic footwall and foreland, in Tollo, R.P., Bartholomew, M.J., Hibbard, J.P., and Karabinos, P.M., eds., From Rodinia to Pangea: The lithotectonic record of the Appalachian region: Geological Society of America Memoir 206, p. 897–916, doi:10.1130/2010.1206(34).

Willett, S. D., 1992, Dynamic and kinematic growth and change of a Coulomb wedge, in: Thrust tectonics, edited by McClay, K. R., pp. 19–32, Chapman and Hall, New York.